

---

# The Crystalline State of Archaeological Bone Material

Wolfgang W. Schmahl, Balazs Kocsis, Anita Toncala,  
Dominika Wycisk, and Gisela Grupe

---

## Abstract

Isotope studies on archaeological bone mineral require a validation of the investigated sample material. Diagenetic alteration or contaminated bone mineral should be recognized as such and not be used for conclusions requiring pristine material. X-ray diffraction (XRD) and Fourier Transform Infrared Spectroscopy (FTIR) provide two complementary tools to characterize the state of the bone mineral. While IR measurements are easy and rapid, their interpretation is still largely empirical. Modern XRD analysis is more demanding with respect to experiment and data evaluation, but it is based on rigorous theoretical modelling of the observed data. Our study involved both uncremated animal bone samples from the alpine region covering ages from 7600 to 550 years before present, as well as cremated human bone remains in comparison with experimentally cremated bovine bone. All samples were mechanically cleaned to remove soil, and inner and outer periosteal surfaces were mechanically removed. We avoided visually decomposed bones completely. The mineralogic state of the thus cleaned, uncremated samples showed only minor systematic changes with archaeological age. The changes are most pronounced for the lattice parameter and crystalline domain size in the short dimension of the original bone-apatite platelets. The long direction corresponding to the crystallographic c-axis of the apatite appears almost unaffected. We conclude that in the investigated samples, there is only a minor diagenetic alteration of the original bone mineral, possibly related to exchange of carbonate by hydroxyl or fluorine.

---

W.W. Schmahl (✉) • B. Kocsis  
Sektion Kristallographie, Ludwig-Maximilians-Universität, Munich, Germany  
e-mail: [Wolfgang.W.Schmahl@lrz.uni-muenchen.de](mailto:Wolfgang.W.Schmahl@lrz.uni-muenchen.de)

A. Toncala • D. Wycisk • G. Grupe  
Biozentrum, Ludwig-Maximilians-Universität, Martinsried, Germany

From annealing experiments with bovine femur bone material at different temperatures for 1 h annealing time, we established calibration curves to be used to estimate cremation temperatures of bones based on FTIR spectra and X-ray diffractograms. While the evaluation of the diffractograms is rigorously based on a physical model, the evaluation of spectral components in FTIR spectra is empirical. The experiments indicate that original bone apatite contains little—if any—OH<sup>-</sup> such that it is carbonate-H<sub>2</sub>O-apatite (rather than hydroxyapatite), and with increasing temperature, water and carbonate leave the material, and from 600 °C, hydroxyapatite is formed with increasing purity and crystallite size with increasing temperature. The analysis of some cremated bones from Urnfield Culture sites of Eching and Zuchering, southern Bavaria, clearly indicated that the archaeological cremated bones are inhomogeneous materials where different parts of the samples were subjected to different cremation temperatures and/or times at temperature within fractions of centimetres. This can be attributed to the conditions in the pile of burning logs and burning tissue. Nevertheless, a fair estimation of cremation temperatures is certainly possible even where the FTIR approach and the XRD approach still do not have a full mutual consistency. Future work needs to address the anatomical variability of original bone material within and between species in much more detail than is known at present. Beyond the well-defined temperature/time conditions in furnace annealing experiments, cremation experiments with bone material analyses must also be done in more realistic conditions as they occur in a funeral pyre.

---

## Introduction

The creation of a map of isotope signatures of archaeological vertebrate bone finds excavated along the Inn-Eisack-Adige passage via the Brenner Pass in the European Alps has been at the core of the initial period of the DFG Forschergruppe FOR1670 (see Introduction). This map is intended to function as a basis to reconstruct ancient migration, trade and culture transfer across this region by geochemical analysis of human bone remains. Certainly, any reliable interpretation of isotopic or microchemical signatures of archaeological bone samples relies on the assumptions that the analysed material is the uncontaminated original material and that this material has been chemically preserved as it was during the life of the individual. The bioapatite bone mineral, however, represents a biogenic tissue component with a specific chemistry and nanostructure that is quite different from that of nominally similar inorganic apatite minerals that are in equilibrium with the ambient conditions where the bone is buried. This, aside from the trivial possibility of contamination with soil particles and the effects of the decomposition of the organic component of the bone, makes bioapatite susceptible to chemical and structural alterations occurring after the death of the individual as the material reacts towards equilibrium with the environment. To take precautions against these possible sources of error in isotope data, FOR1670 decided to screen the

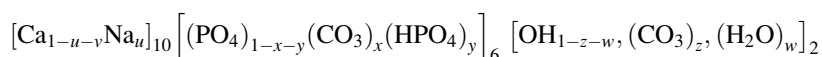
archaeologic bone finds by mineralogic analysis based on X-ray diffraction and infrared spectroscopy. In a time period of about 1500 years in the investigated area, from the Bronze Age until Imperial Roman Times, i.e. 60 generations, cremating the deceased was the dominant burial custom (Grupe et al. 2015). Thus, we performed some initial analyses on cremated bones to prepare for a deeper study in the second funding period of FOR1670.

## The Bone Mineral

Bone is a composite material of nearly equal volumes of collagen and nanometre scale crystallites of a carbonated apatite mineral (Peters et al. 2000). The geologic mineral hydroxyapatite is rarely found, as the geologic apatite tends to incorporate  $F^-$  and  $Cl^-$  ions instead of  $OH^-$  to give an approximate formula  $Ca_{10}(PO_4)_6(F_{1-x-y}, Cl_x, OH_y)_2$ . Bone has a complex hierarchical structure (Wegst et al. 2015; Reznikov et al. 2014; Schwarcz et al. 2014; Weiner et al. 1999; Rho et al. 1998) where the platelike nanocrystals of  $\sim 2 \times 30 \times 40$  nm size (Cuisinier et al. 1987; Alexander et al. 2012) provide stiffness and compressive strength to the hybrid composite.

The formation of the apatite mineral phase is a complex, biologically controlled process, where the mechanisms of nucleation, growth and growth limitation of the small crystallites are not yet clear. There are several models, including other calcium phosphate phases as precursors and growth from an amorphous phase (Landis and Jacquet 2013).

Chemically, the apatite mineral component of the mammal bone can be approximated as



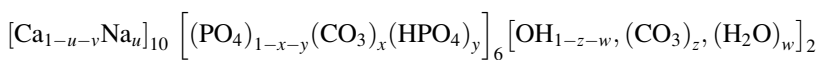
where the small potential vacancy concentration  $v$  on Ca-sites is

$$v = 3(x+y) - z + w - \frac{1}{2}u; (x, y, z, u, v, w \geq 0).$$

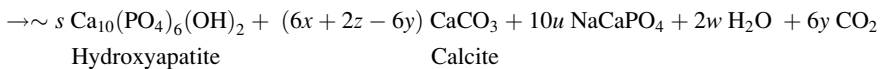
Carbonate (5–8 wt.%) is an essential component of the bone mineral, mostly substituting for  $[PO_4]^{3-}$ , but also for  $[OH]^-$  to a much lesser degree (LeGeros et al. 1967, 1968; Rey et al. 1989, 1990, 1995; Yi et al. 2013). The two different variants of  $[CO_3]^{2-}$  substitution in the crystal structure (type A  $[CO_3]^{2-} \leftrightarrow [PO_4]^{3-}$ , type B  $[CO_3]^{2-} \leftrightarrow [OH]^-$ ) (Wopenka and Pasteris 2005) can be distinguished by IR spectroscopy (Balan et al. 2011). The presence of the acidic phosphate species  $[HPO_4]^{2-}$  is also important in the biomineral (Wang et al. 2013; Rey et al. 2014). For bone apatite, the presence of  $OH^-$  is low (Pasteris et al. 2004), and water may reside in the OH position. A multitude of different schemes of coupled exchange to maintain charge balance can be suggested (e.g. Wopenka and Pasteris 2005; de Leeuw 2010). In mammal bioapatite, small amounts of  $F^-$  replace  $OH^-$  (notably in tooth enamel), and on the  $Ca^{2+}$  cation position voids (Wilson et al. 2005),  $Na^+$  and  $Mg^{2+}$  can be substituted as well as traces of  $Sr^{2+}$  and  $Ba^{2+}$  (e.g. Elliot 2002; Turner-

Walker 2008). Sponheimer et al. (2005) report that herbivores accumulate higher levels of  $\text{Sr}^{2+}$  und  $\text{Ba}^{2+}$  than carnivores and omnivores.

Nuclear magnetic resonance investigations of Jäger et al. (2006) and Wang et al. (2013) indicate the existence of an amorphous surface layer of water-bearing carbonated Ca-phosphate (amorphous calcium carbonate, ACC) which coats a bioapatite nano-crystallite core. Together with the collagen and other organic/cellular components, the mineral nanoparticles compose, right from the supramolecular scale, a hierarchical hybrid composite (Wegst et al. 2015; Reznikov et al. 2014; Schwarcz et al. 2014; Weiner et al. 1999; Rho et al. 1998). As long as this compound structure remains intact, both the inorganic and the organic components are stabilized against chemical and biochemical attack (Gernaey et al. 2001; Turner-Walker 2008). The taphonomic (biological postmortem) decomposition of the about 30 wt.-% organic components of the bone (Peters et al. 2000) creates a high porosity and internal surface in the remaining mineral. This internal surface is reactive and promotes adsorption of ions and molecules from solutions in the soil. The triangular  $[\text{CO}_3]^{2-}$  groups which are substituted into the crystal structure for the tetrahedral  $[\text{PO}_4]^{3-}$  complex or for the essentially spherical  $\text{OH}^-$  induce structural disorder related to the geometric mismatch and charge compensation mechanism. Both this structural misfit and the high surface/interface area increase the free energy of the bioapatite, and thus it has an increased solubility compared to inorganic hydroxyapatite, which is fairly insoluble (Hedges 2002; Berna et al. 2004; Wopenka and Pasteris 2005; de Leeuw 2010). In vivo this enhanced solubility plays a substantial role in the continual physiologic reconstruction of bone. Similarly, the increased free energy provides a driving force for diagenetic recrystallization (Nielsen-Marsh and Hedges 2000; Nielsen-Marsh et al. 2000) and formation of larger crystals. Thus, secondary minerals may form such as newly grown abiotic inorganic hydroxyapatite (which is free of carbonate) and calcite,  $\text{CaCO}_3$ , taking up the  $[\text{CO}_3]^{2-}$  and associated  $\text{Ca}^{2+}$  from the former bioapatite.



Bioapatite (Carbonate-Hydro-Hydroxyapatite)



with  $s \approx (1 - 2u - v - 0.6x - 0.2z + 0.6y)$ .

The  $\text{NaCaPO}_4$  phase here is a nominal phase to account for the sodium. Those secondary minerals potentially incorporate ions present in the soil solution, such as  $\text{Sr}^{2+}$ ,  $\text{Pb}^{2+}$ , etc. (Tütken et al. 2008), which changes the trace elements signatures of the sample.

While the bone mineral is comparatively stable against exposures at temperatures reached by cooking, boiling, or roasting, conditions above ca. 500 °C profoundly change the bulk chemistry and crystalline consistence of the bioapatite (Rogers and Daniels 2002; Enzo et al. 2007; Munro et al. 2008; Piga et al. 2008, 2009a, b, 2013;

Harbeck et al. 2011; Galeano and Garcia-Lorenzo 2014). From about 500 °C, a significant recrystallization of the bioapatite and crystallite growth of hydroxyapatite sets in. Prehistoric cremation pyres could reach temperatures up to 1000 °C (McKinley 2016). Ratios of stable isotopes of light elements contained in the atmosphere change considerably during heat treatment (Olsen et al. 2008; Schurr et al. 2008), while those of elements such as strontium and lead do not appear to be altered as long as there are no reactions with surrounding materials (Harbeck et al. 2011).

The selected techniques for mineralogical characterization of the bone materials, X-ray diffraction (XRD) and Fourier Transform Infrared Spectroscopy (FT IR), are essentially complementary. To characterize the diagenetic recrystallization of bone apatite, Person et al. (1995) defined their classical empirical “crystallinity index” (CI) on the basis of the width of X-ray diffraction lines. This index number became widely used (e.g. Hedges 2002). Another popular empirical index number is the infrared splitting factor (IRSF) by Weiner et al. (1993) (see, e.g. Surovell and Stiner 2001). The utility of the simple IRSF to describe complex spectral features is debated in the literature (Sillen 1989; Shemesh 1990; Weiner and Bar-Yosef 1990; Wright and Schwarcz 1996; Trueman et al. 2008; Tütken et al. 2008). According to Shinomiya et al. (1998), the IRSF indicated chemical alterations already a few years after death. Sample preparation for XRD or FTIR measurement certainly has an influence on the CI/IRSF results (Surovell and Stiner 2001). The simplifying indices for a “crystallinity” of the bone mineral do not correlate with modifications of chemical composition and also not with stable isotope data of the structural carbonate (e.g. Lee-Thorp and Sponheimer 2003; Pucéat et al. 2004; Trueman et al. 2008; Tütken et al. 2008). Moreover, physiological differences in bioapatite characteristics between different species, different skeletal elements and different age groups of the population can be expected and need to be considered in the future (Rey et al. 1991, 2009; Yerramshetty and Akkus 2008). To put the IRSF on a more physical basis, Lebon et al. (2008) suggested spectral decomposition by curve-fitting procedures on the relevant part of the infrared spectrum; these procedures were later improved by Vandecandelaere et al. (2012) and Grunenwald et al. (2014). Pedone et al. (2007) and Yi et al. (2014) contributed more rigorous considerations on the theory of phosphate and carbonate vibrations to be expected in bioapatite.

The X-ray diffraction (XRD) technique takes advantage of the periodic lattice-like structure of crystalline materials, as it measures interference patterns of the X-ray waves scattered from the atoms or molecules in the material. Crystals are objects with a spatially periodic arrangement of the constituting atoms, ions or molecules, and for such materials, the interference maxima become sharp if the spatial range of the periodic order is wide. The concept of a crystal is an array of building blocks (called unit cells, Fig. 1) which are periodically repeated in a space-filling, lattice-like fashion. The positions of the X-ray diffraction peaks are defined by the unit-cell dimensions, the so-called lattice parameters. The peak intensities, explained in a nutshell, are related to the electron density distribution pattern in the unit cell averaged over time and space in the crystal. This pattern reflects the positions and electron densities of all the individual atoms or molecules in the crystal, superimposed by the space and time average (cf. for details e.g. to

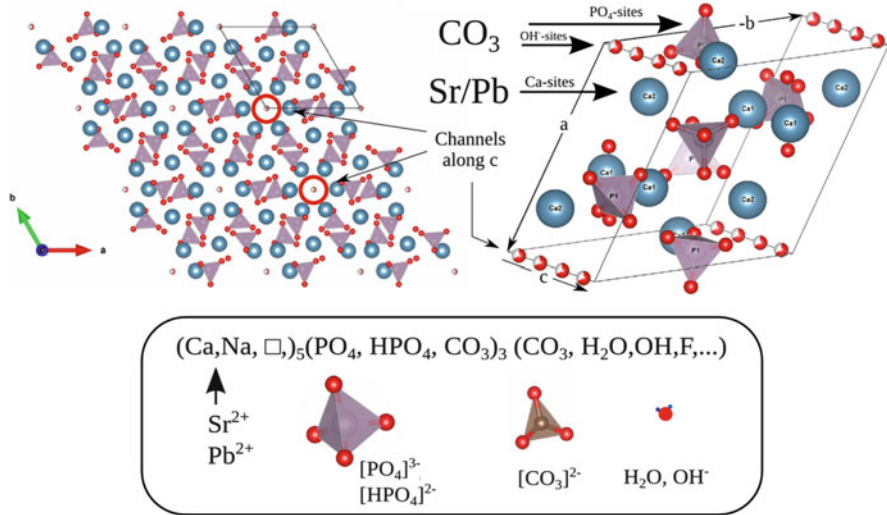


**Fig. 1** Crystal structure of hydroxyapatite in hexagonal setting after Wilson et al. (1999) and Tonegawa et al. (2010). Some authors (Ikoma et al. 1999; Tonegawa et al. 2010) believe that monoclinic symmetry (space group  $P2_1/c$ ) gives a better description for well-crystalline hydroxyapatite. In bioapatite, the  $[\text{PO}_4]^{3-}$  is exchanged by  $[\text{CO}_3]^{2-}$  and  $[\text{HPO}_4]^{2-}$ , while the channel sites ( $\text{OH}^-$  location of hydroxyapatite) contain  $[\text{CO}_3]^{2-}$ ,  $\text{H}_2\text{O}$ ,  $\text{OH}^-$  and other ions. The Ca-sites are also occupied by minor amounts of  $\text{Na}^+$  and by vacancies (*white square*). It is here where trace elements such as  $\text{Sr}^{2+}$  and  $\text{Pb}^{2+}$  reside

Pecharsky and Zavalij 2003 and Mittemeijer and Welzel 2012). For small crystallites, as is the case for bioapatite, there are fewer atoms contributing to the interference phenomenon, and thus the diffraction maxima widen inversely proportional to the coherence length of the periodic crystalline order (de Keijser et al. 1982). The width and shape of the X-ray diffraction peak related to a particular lattice plane depend both on this coherence length (i.e. in the simplest case the crystallite size) perpendicular to that plane and on the variance of the lattice parameters in the sample, the so-called microstrain. Microstrain results from inhomogeneities in chemical composition, other lattice defects, and from mechanical strains on the scale of the crystallite size. In the case of bone, such mechanical strains can result from the composite structure with collagen. Note that the frequently used term “crystallinity” (Rogers et al. 2010) is a notion mingling effects of crystallite size, microstrains, random chemical substitution and presence of amorphous phases in a rather undefined way.

Deviations from the average structure give a very small intensity contribution in XRD, which we neglect here. Amorphous substances do not have a periodic structure; their diffraction pattern consists of diffuse intensity halos with maxima related to peaks in the spatial probability density distribution of the constituting atoms. In any case, amorphous, crystalline or “in between”, the diffraction signal is the Fourier transform of the electron density self correlation function, which is straightforward to calculate (see Schmahl et al. 2016 for more information). Thus,

modern XRD analysis is based on a rigorous calculation of the diffraction profile and algorithms fitting the model parameters to obtain the best-possible agreement with the observed diffraction profile (so-called Rietveld refinement method, Rietveld 1969; Rodriguez-Carvajal 1993; Rodriguez-Carvajal and Roisnel 2004; Pecharsky and Zavalij 2003; Mittemeijer and Welzel 2012).

This quantitative treatment of the X-ray diffraction profile led to assessments of the crystallographic characteristics of archaeological and paleontological bone materials (Stathopoulou et al. 2008; Piga et al. 2008, 2009a, b, 2013; Harbeck et al. 2011). Stathopoulou et al. (2008) examined Miocene and Pleistocene samples from the Aegean with the Rietveld technique and arrived at the conclusion that “Diagenetic trends, common to all these sites include a subtle but systematic decrease of the unit-cell volume and a-axis of carbonate hydroxylapatite, as well as a parallel increase of the coherence length along the c-axis”. Stathopoulou et al. (2008) also established a correlation of X-ray diffraction data with IR data. Enzo et al. (2007), Piga et al. (2008, 2009a, b, 2013), Harbeck et al. (2011), and Galeano and Garcia-Lorenzo (2014) applied modern full-profile analysis of X-ray diffractograms to evaluate effects of cremation on the bone mineral. From about 500 °C, a significant recrystallization of the bioapatite and crystallite growth of hydroxyapatite sets in. Piga et al. (2008, 2009a) experimented with varying cremation times at different temperatures and found that between 600 °C and 850 °C, the transformation of the bioapatite to hydroxyapatite occurs essentially within the first 20 min of the heat treatment.

X-ray diffraction is less well suited to probe local molecular environments. Infrared spectroscopy, however, can distinguish, e.g. the two different variants of  $[\text{CO}_3]^{2-}$  substitution in the crystal structure (type A  $[\text{CO}_3]^{2-} \leftrightarrow [\text{PO}_4]^{3-}$ , type B  $[\text{CO}_3]^{2-} \leftrightarrow [\text{OH}]^-$ ) (Wopenka and Pasteris 2005). Infrared spectroscopy (IR) probes the frequencies of molecular scale vibrations in the material. Infrared photons are absorbed if their frequency is in resonance with a frequency of a molecular scale vibration in the sample. The frequency characteristics of the vibration depend on the precise local structural configuration of the vibrating entity in the sample. In a crystallographically well-ordered material, the vibrations in neighbouring unit cells are identical. In this case, the IR absorption peaks are well developed and rather sharp. In a disordered or amorphous material, the IR absorption signal is still present, but it broadens as the molecular vibration frequencies become locally different due to different molecular environments in the structure. This interaction is complex, however, as the frequencies shift both with changing chemical bond strengths and masses of vibrating bodies in different configurations or environments, but the signal also broadens in relation to the fading (damping) of the vibration after its initial excitation.

In any case, the IR spectrum reflects the time structure of local molecular scale environments of the vibrating entities in the sample, while the X-ray diffraction signal reflects the spatial periodicity in the atomistic structure. Accordingly, the two methods give complementary information. Atoms and molecules vibrate around their equilibrium configuration in all materials, regardless if the materials structure is crystallographically ordered or not. This gives an advantage to IR spectroscopy for the investigation of materials which are not spatially ordered. On the other hand,

IR probes periodic long-range order (“crystallinity”) only indirectly: by the effect of the crystal structure on the time structure of the vibrations. So far, there is no straightforward general way to calculate this indirect influence.

---

## Materials and Methods

Among the uncremated archaeological animal bone samples which were prepared for isotope studies in FOR1670 (see chapter “Isotopic Map of the Inn-Eisack-Adige-Brenner Passage and its Application to Prehistoric Human Cremations”), we selected 63 random samples for screening by X-ray diffraction. The samples were from the species *Bos taurus*, *Sus domesticus* and *Cervus elaphus*. Fresh bovine bone samples and fossil samples of a Miocene hippopotamus from Bavaria were obtained for comparison. A piece of compact bone was cut from the skeletal element, and the endosteal and periosteal surfaces were mechanically removed by grinding off. The sample was then ultrasonically washed in deionized H<sub>2</sub>O (35 kHz), where the water was changed every 5 min. The washing was repeated until the water remained clear. After drying in air, the bone piece was defatted for 5 h with diethylether in a Soxhlet and air dried again. Finally, the sample was homogenized to a fine powder.

For experimental cremation, we used thus prepared bovine femur powder and subjected it to heat treatment in air in a muffle. The samples were put into the preheated furnace for an exposure time of 1 h, after which they were removed and left to cool in air.

For an investigation archaeological bone samples from burials which were subjected to cremation as a burial rite, we selected long bones from the Bronze Age (Urnfield Culture) site of Eching (1300–800 BC) and a skull from the Zuchering site of the same culture, both in southern Bavaria. All cremated bones were buried in urns; the urns were found in a broken state.

X-ray diffractograms were collected on a General Electric 3003 powder diffractometer in Bragg-Brentano reflection geometry. Cu-K $\alpha_1$  radiation was selected with a focussing monochromator in the primary beam. Data collection time for a complete diffractogram from 5 to 100 degrees  $2\theta$  amounted to 240 min with a 1D Meteor detector and exposure time of 1000 s for each frame. The instrumental resolution function was experimentally determined with a NIST LaB<sub>6</sub> standard. For data evaluation and Rietveld refinement, the FULLPROF code (Rodriguez-Carvajal 1993; Rodriguez-Carvajal and Roisnel 2004) was employed. The Thompson-Cox-Hastings method for convolution of sample effects such as anisotropic size and isotropic microstrain broadening (Thompson et al. 1987) with instrumental resolution (as determined with a NIST LaB<sub>6</sub> standard) was applied.

Infrared spectra were measured on a Bruker Equinox FTIR instrument with a resolution of 4 cm<sup>-1</sup>. A total of 128 scans was averaged resulting in a 2 min acquisition time per sample. The bone powder (as described above for XRD) was sieved through a 100  $\mu$ m mesh, and 1 mg of resulting sample powder was manually mixed with 200 mg of KBr in a mortar and pelletized subsequently. Spectral decomposition into seven bands was performed in the range 400–800 cm<sup>-1</sup>. The seven bands were fitted with a Gaussian-Lorentzian sum function with fixed ratio of



3:7 each. For each band, the center position, the full width at half maximum (FWHM) and the peak area were fitted. Background was described with a cubic polynomial, but the function remained essentially flat.

## Results and Discussion

### The Uncremated Mammal Bones

Due to the nanoscale dimension of the bone bioapatite particles, the diffraction peaks of original bone material are significantly broadened (Fig. 2). The broadening is anisotropic, as the (002) peak, corresponding to the crystallographic c-axis of the crystallites, is comparatively sharp while the peaks corresponding to the a- and b-directions are significantly broader. We parameterized the size as a second rank tensor, corresponding to an ellipsoid. The agreement between observed and calculated diffraction profile is excellent in view of the complexity of the system. Due to

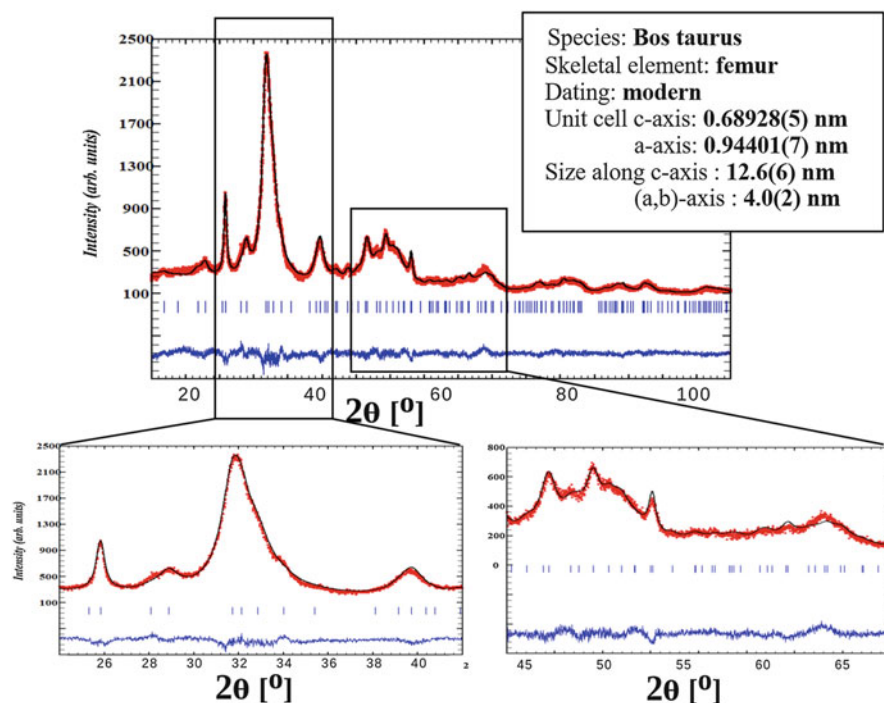


**Fig. 2** X-ray diffraction trace of the bone mineral from the femur of modern domestic cattle (*Bos taurus*) taken with  $\text{Cu-K}\alpha_1$  radiation. Red dots: observed data points; black line: calculated XRD profile; blue line on bottom: difference of observed and calculated data. Blue vertical bars: positions of the diffraction peaks. The two enlarged regions show the most featured parts of the diffractogram. The XRD profile was fitted with an anisotropic size model for the coherently diffracting domain

the hexagonal symmetry, the XRD peaks which would have been able to discriminate different crystallite sizes in a- and b-directions directly overlap, so that a distinction is not possible with the current method. Correspondingly, quoted crystallite sizes correspond to an average of the directions in the a-b plane. For the fresh bovine bone, we arrive at 12.6 nm for the c-direction and 3.9 nm for the a-b plane. The estimated precision of these numbers from the Rietveld least-squares fit is in the order of 5 %. Most of the archaeological samples show a slightly reduced broadening such that the 211, 121, 112 and 030 peaks become more distinct (Fig. 3). This may indicate grain growth and/or dissolution of the finest-scaled fraction during burial. Most importantly, we observe calcite as a secondary phase in about 20 % of the investigated archaeological sample. Note that all investigated samples had visually very good quality to be selected for isotope analysis, and their surfaces were cleaned away to avoid contamination by soil. There is no indication of typical soil minerals such as clay minerals or quartz, other than calcite, such that the selection and cleaning procedure was effective. Only in 3 samples out of 63, the determined calcite fraction was  $\geq 2$  wt.%, with the maximum at 5 wt.%. The

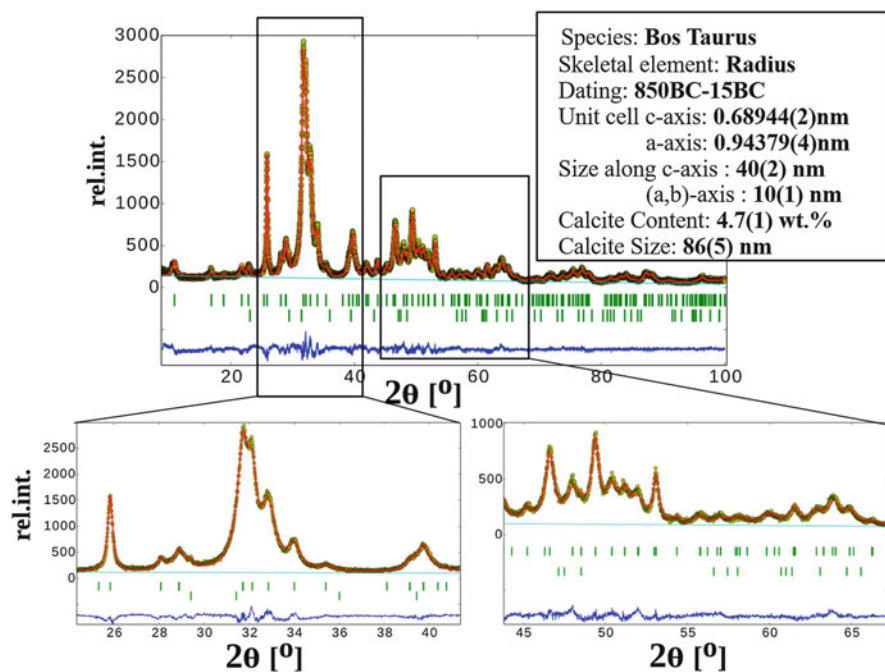


**Fig. 3** X-ray diffraction trace of an archaeological animal bone sample (*Bos taurus*, radius) from the Brixen Stufels, Hotel Dominik site. Cu- $\alpha_1$  radiation. Red dots: observed data points; black line: calculated XRD profile; blue line on bottom: difference of observed and calculated data. Green vertical bars: positions of the diffraction peaks; top row: bone apatite; bottom row: calcite. The two enlarged regions show the most featured parts of the diffractogram. The XRD profile was fitted with an anisotropic size model for the coherently diffracting domain. In the enlarged region the different broadening of the 002 and the 030 peaks can be clearly seen (c.f. Fig. 5)

observed calcite itself shows a diffraction line broadening which indicates a crystallite size on the scale of 100 nm, which is a strong indicator that this calcite is not simply due to crystallization from infiltrating soil solution, for which micrometre-sized crystals would be expected. We examined an archaeological deer bone (metatarsus) in the SEM after careful deproteination (Fig. 4). The calcite is contained inside the bone fabric in the form of ideal rhombohedral crystals of the 100–500 nm size range.

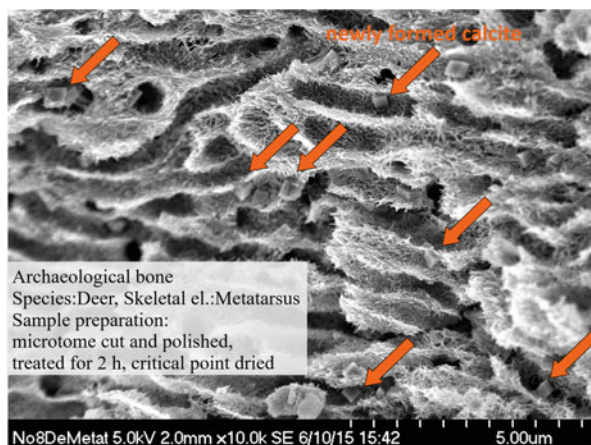


**Fig. 4** SEM micrograph of deproteinated archaeological deer bone (metatarsus) from the Brixen-Stufels “Hotel Dominik” 4856 archaeological site (~ 5th century BC). Note the ideal rhombohedral crystals of secondary calcite (*arrows*) distributed in the bone fabric

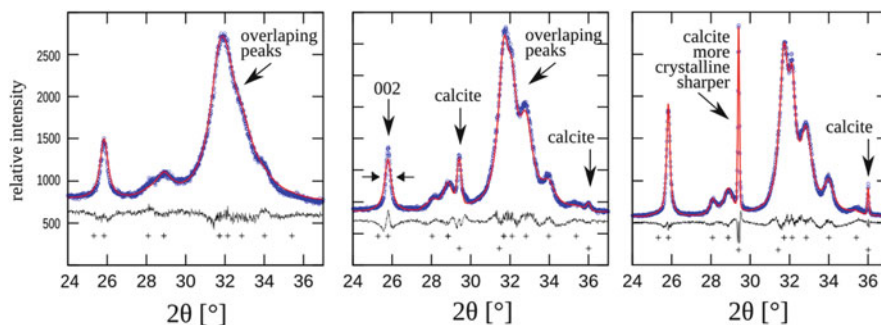


**Fig. 5** Comparison of the 25°–42°  $2\theta$  range of X-ray diffractograms of fresh bone (*Bos taurus*, femur) and two archaeological bones (*Sus domesticus*, mandibula, *Cervus elaphus*, metatarsus III +IV). Cu- $k\alpha_1$  radiation. *Blue dots*: observed data points; *red line*: calculated XRD profile; *black line on bottom*: difference of observed and calculated data. *crosses*: positions of the diffraction peaks; *top row*: bone apatite; *bottom row*: calcite

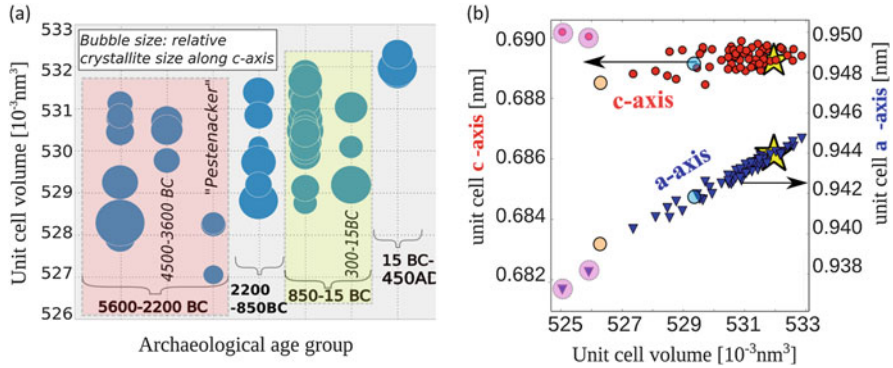


**Fig. 6** Overview on crystallographic parameters of the uncremated archaeological samples of animal bones. **(a)** Unit-cell volume vs. archaeological (cultural) age group. The bubble size indicates the size along  $c$  of the coherently diffracting domain. There is only a weak correlation with archaeological age. **(b)** Lattice constants (unit-cell axes) vs. unit-cell volume. *Red dots and blue triangles*: unit cell  $c$ -axis and  $a$ -axis, respectively, of the archaeological bones. *Yellow stars*: modern bovine femur. *Pink circles*: Miocene ( $\sim 20$  million year old) fossil hippopotamus from Bavaria. *Light blue circles*: hydroxyapatite. *Orange circles*: fluorapatite

A closer comparison of the  $25^\circ$ – $42^\circ$  diffraction angle ( $2\theta$ ) range is shown in Fig. 5. There is a small but detectable sharpening of the XRD peaks of the archaeological material compared to the fresh bovine femur.

Figure 6 gives an overview on crystallographic parameters of the 63 examined archaeological samples. Figure 6a compares the apatite unit-cell volume and the crystallite size along the  $c$ -axis with the archaeological age group. We observe only a vague correlation of unit-cell volume decreasing with archaeological age, and the crystallite size shows no correlation with age. Clearly, this indicates that there are other factors contributing to the measured lattice parameter than just changes with age, related to possible loss of carbonate. These other factors may include humidity and soil pH at the archaeological site, which might affect the alteration reaction, and also intraspecies and across-species variations of the crystallographic parameters of the bone mineral, which still need to be examined in the future. Figure 6b displays the lattice parameters and unit-cell volume. The star in Fig. 6b marks the lattice parameters of the fresh bovine femur bone material. The pinkish circles mark the lattice parameters of a bone fragment of a fossil Miocene hippopotamus from Bavaria ( $\sim 20$  million years old). The plot of Fig. 6b allows to conclude that the  $c$ -axis of the archaeological bone mineral is fairly constant while the  $a$ -axis lattice parameter varies in a systematic way. The data lie on a pseudo-linear trend (because the unit-cell volume  $V$  scales with the lattice parameters as  $V = a^2c \sin 120^\circ$ , and the parabolic relation between  $V$  and  $a$  is approximately linear in a small range of data), but interestingly, this trend line connects the fresh bone with the fossil bone. Synthetic hydroxyapatite also lies on this trend line (light-blue circle) and fluorapatite (orange circles) as well. We infer that the bone mineral undergoes a chemical alteration during burial, possibly by exchange of the carbonate with hydroxyl and fluorine. But this interpretation needs to be confirmed with future studies.

**Fig. 7** Correlation of unit-cell volume with microstrain broadening. Microstrain is the statistical variation of the lattice parameters due to chemical or mechanical inhomogeneity in the sample. Smaller unit-cell volumes, indicative of higher degree of diagenesis, are associated with larger inhomogeneity of the lattice parameters in the sample

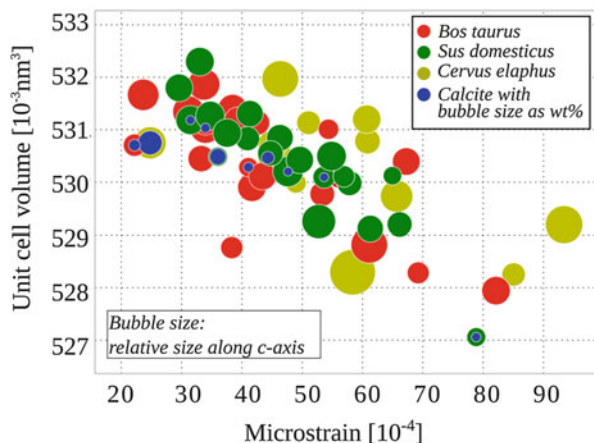
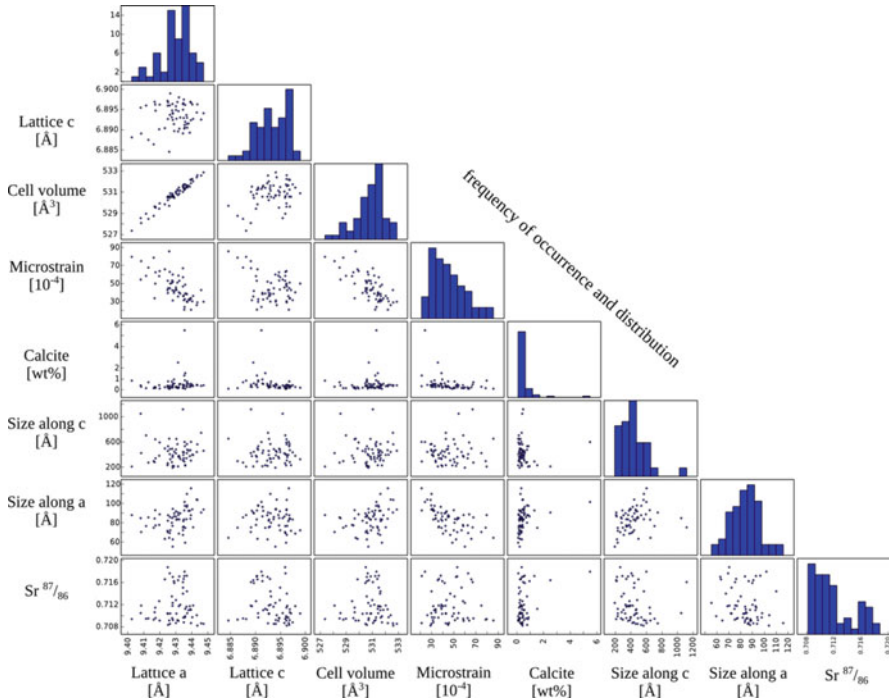


Figure 7 plots the unit-cell volume vs. the distribution width of the statistical variation of lattice parameters within each single sample (the so-called microstrain), which also gives a diffraction line broadening, which can be distinguished, however, from the size broadening to its different dependence on the scattering angle ( $\tan\theta$ ) compared to the size broadening  $(\cos\theta)^{-1}$ . There is a correlation indicating that smaller unit cells, which appear to occur due to alteration by loss of carbonate, as discussed above, have a more inhomogeneous distribution of lattice parameters. This can be explained by an inhomogeneity in the progress of the alteration reaction within each bone sample. However, the plot also indicates that the three different species which were examined show different characteristic, with the wild form (*Cervus elaphus*) displaying a larger spread than the domesticated species (*Sus* and *Bos*).

Figure 8 displays a compilation of crystallographic parameters and  $^{87}\text{Sr}/^{86}\text{Sr}$  isotope values for the 63 samples. It shows that the data set is fairly uniform with any correlations occurring in a quite random manner. We interpret this situation as due to the successful cleaning procedure, which removed potential contamination, and that in the selected material, the isotope ratios do not show any trends with the crystallographic parameters of the bone apatite.

## Furnace Annealing (Experimental Cremation)

To simulate the effect of heat treatment on bone material, we performed annealing experiments with bovine femur material. Figure 9a gives an overview of the change of the bone mineral diffractograms as a function of annealing temperature; Fig. 9b and c show sections of the diffractograms as difference plots between measured and calculated profile. Below 400 °C, the width of the peaks reduces only little, but we see small but significant changes of the lattice parameters (Fig. 10). These could be the result of the breakdown of the collagen and the changes in the composite structure of the bone occurring accordingly. Between 400 °C and 600 °C, the trend in the lattice parameters is reversed compared to the lower temperatures, indicating that a different and so far unknown structural process sets in. From about 600 °C upwards, there is a marked



**Fig. 8** Scattergram of the most relevant crystallographic parameters (from Schmahl et al. 2016)

increase in sharpness of the XRD peaks, which is related to a dramatic increase of the crystallite size and a progressive transformation from carbonated apatite to hydroxyapatite as a function of annealing temperature (Fig. 10; Table 1). Similar results have been obtained by Rogers and Daniels (2002). CaO forms as a further reaction product of the bioapatite decomposition at 800 °C and above.

Infrared spectra of the cremated bioapatite are shown in Figs. 11, 12 and 13. Figure 11 compares a typical IR spectrum of archaeological bone with those of two selected experimentally annealed bones. The archaeological bone—like fresh bone—shows carbonate vibration bands. Their intensity decreases with heat treatment, and they are absent in the material annealed at 1000 °C, which shows the spectrum of hydroxyapatite. In Fig. 12, spectral changes with heat treatment are shown, in particular, the development of the OH<sup>-</sup> stretching vibration at 3568 cm<sup>-1</sup> and the OH<sup>-</sup> libration near 633 cm<sup>-1</sup> as a function of heat treatment. It is very evident that the contributions of OH<sup>-</sup> to the spectra of untreated bone are quite insignificant and that they rise with heat treatment. This can also be seen in the FTIR spectra of Stiner et al. (1995). Further, the deproteinated untreated bone shows an intense contribution of H<sub>2</sub>O, which diminishes with heat treatment and which is practically absent in the sample treated at 1000 °C. This all points to the assumption that the bioapatite is a carbonate-H<sub>2</sub>O-apatite with little OH<sup>-</sup> (Rey et al. 1995; Loong et al. 2000; Pasteris et al. 2004) and it becomes hydroxyapatite with



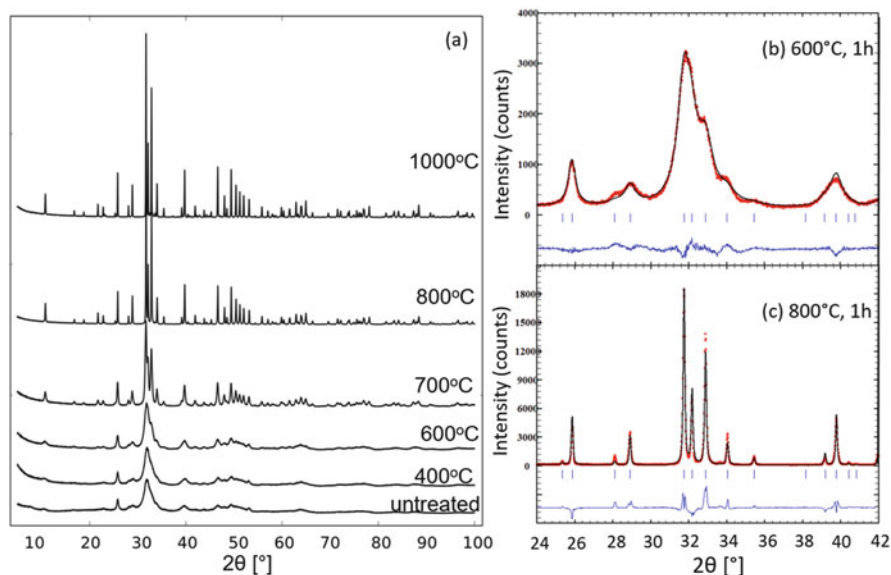


**Fig. 9** Overview of X-ray diffractograms of bovine femur bone mineral samples annealed for 1 h at different temperatures (experimental cremation). Note the dramatically increasing sharpness of the XRD peaks with annealing temperatures above 600 °C corresponding to increasing crystallite size. Exemplary Rietveld fits are shown in (b) and (c) for treatment at 600 °C and 800 °C

heat treatment, losing  $\text{CO}_2$  and perhaps some  $\text{H}_2\text{O}$  ( $\text{CO}_3^{2-} + \text{H}_2\text{O} \rightarrow \text{CO}_2 + 2\text{OH}^-$ ). At the same time, the high temperatures lead to an increased crystallite size by Ostwald-ripening, driven by the reduction of free energy by lowering the internal surface. The excess free energy due to the surface is proportional to  $(2\gamma/r)$  where  $\gamma$  is the specific surface energy and  $r$  is the crystallite size; thus, large crystallites grow at the expense of smaller crystallites.

Figure 13 displays the spectral decomposition based on seven peaks in the 400–800  $\text{cm}^{-1}$  range which covers the  $\nu_4$  phosphate group bending modes and the mode at 633  $\text{cm}^{-1}$  which is attributed to  $\text{OH}^-$  libration (Gonzalez-Diaz and Hidalgo 1976; Gonzalez-Diaz and Santos 1977; Vandecandelaere et al. 2012). The most robust spectral parameter useful to correlate with cremation temperature is the full width at half maximum (Balan et al. 2011) of the band at 603  $\text{cm}^{-1}$ . It correlates linearly with cremation temperature (Fig. 14). For uncremated bones and for low temperatures of heat treatment, the FTIR peaks are poorly developed and show a large overlap of the spectral features (Figs. 13a and 14). As the material gets more ordered while it approaches more stoichiometric chemistry with increasing sintering temperature, the peaks get increasingly narrower and well defined. The calibration equation is

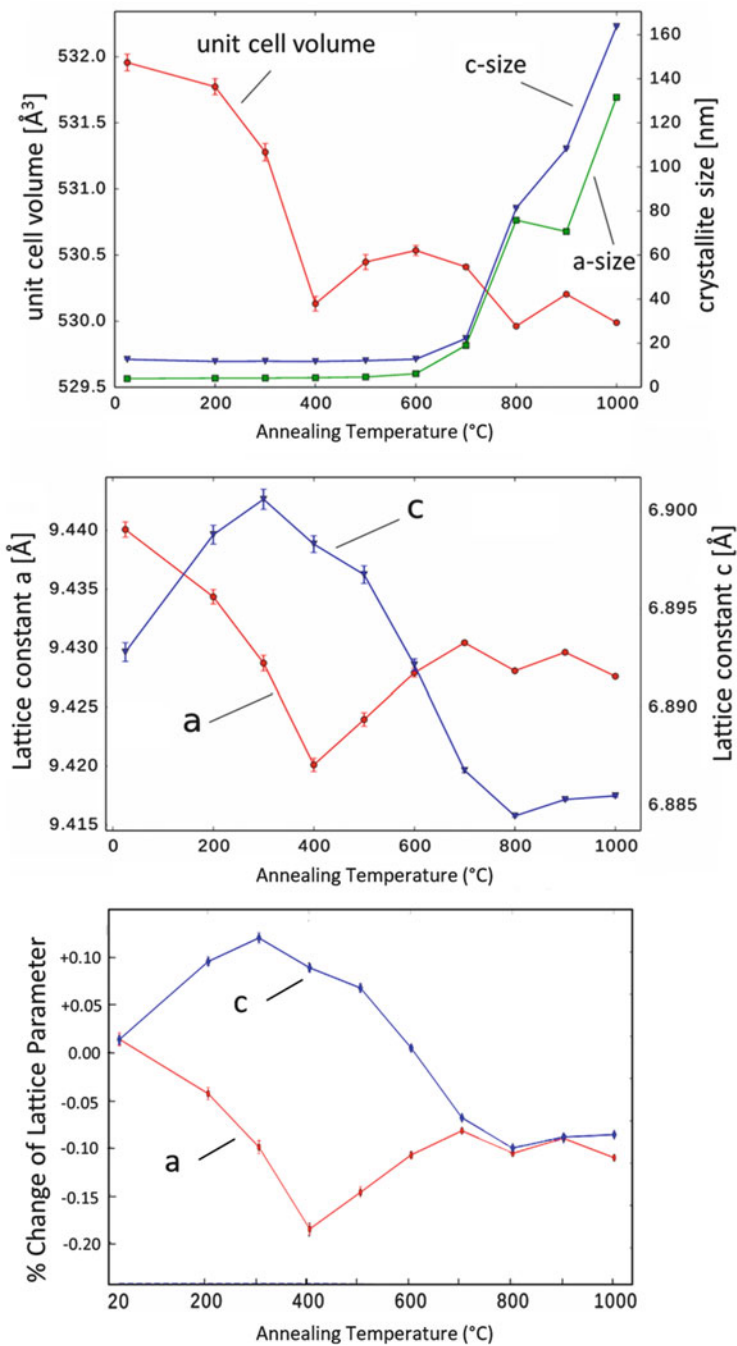


**Fig. 10** Size of the coherently diffracting domains in c- and a- and b-direction (crystallite sizes labelled “c-size” and “a-size”, respectively) and lattice parameters for the experimentally annealed samples as a function of annealing temperature. Annealing time is 1 h



**Table 1** X-ray diffraction results on experimentally annealed samples and cremated archaeological samples

Experimentally annealed samples				
Annealing temperature (°C)	<i>c</i> (Å)	<i>a</i> (Å)	<i>c</i> -size (nm)	( <i>a,b</i> )-size (nm)
21	6.8854(5)	9.4318(7)	12.7	3.9
200	6.8876(5)	9.4234(7)	11.7	4.1
300	6.8932(5)	9.4218(7)	11.8	4.2
400	6.8912(4)	9.4161(6)	11.7	4.3
500	6.8921(4)	9.4231(5)	12.1	4.6
600	6.8899(3)	9.4266(4)	12.7	6.1
700	6.88718(11)	9.4303(12)	22.1	19.0
800	6.88486(5)	9.42865(6)	81.2	75.8
900	6.88616(6)	9.43106(7)	108.2	70.6
1000	6.88601(5)	9.42822(5)	163.7	131.5
Eching samples				
8_Eching_247	6.891953(18)	9.41861(20)	104	93
10_Eching_626	6.8836(7)	9.44582(9)	128	44
14_Eching_727	6.89629(12)	9.41812(17)	22.5	11.5
17_Eching_346	6.88568(3)	9.42397(3)	113	101
18_Eching_140	6.88682(3)	9.42269(4)	143	98
19_Eching_219	6.88686(2)	9.42079(3)	188	130
20_Eching_222	6.89439(14)	9.4198(2)	22.5	10.2
Zuchering skull				
Outer_1	6.89796(6)	9.42178(8)	69	60
Inner_1	6.89727(14)	9.4221(2)	36	22
Outer_2	6.89857(4)	9.42311(5)	139	147
Inner_2	6.89603(5)	9.42419(6)	173	108
Outer_3	6.89873(5)	9.4215(6)	73	63
Inner_3	6.89832(16)	9.4211(2)	35	21
Outer_4	6.89772(11)	9.42127(14)	36	27
Inner_4	6.89885(18)	9.4185(2)	23	13
Outer_5	6.89797(8)	9.42159(11)	42	32
Inner_5	6.9004(2)	9.4206(3)	22	12

Numbers in brackets are standard deviations referring to the last digit(s). The estimated standard deviation for crystallite sizes is estimated as 5 %

$$FWHM = -0.0231 \left[ \frac{\text{cm}^{-1}}{^{\circ}\text{C}} \right] * T + 37.9 [\text{cm}^{-1}] \quad (1)$$

where *T* is the cremation temperature in °C.

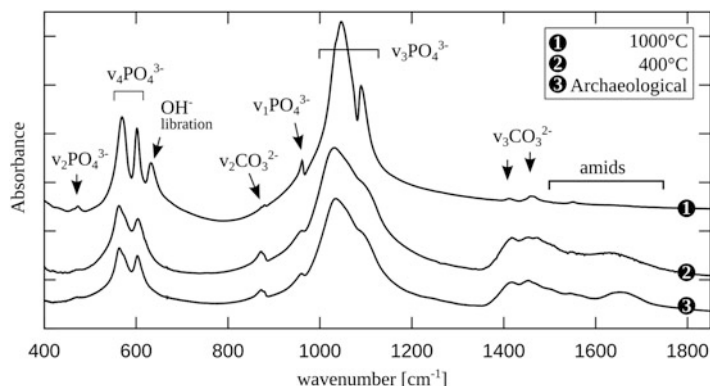


**Fig. 11** Comparison of FTIR spectra of uncremated archaeological and experimentally annealed samples with the most important vibrational bands indicated. Note the absence of carbonate bands in the 1000 °C annealed samples and the absence of OH<sup>-</sup> libration in the uncremated sample and the 400 °C annealed sample

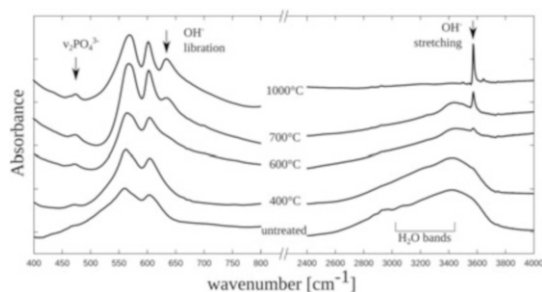


**Fig. 12** Change of the FTIR spectra of degreased and deproteinized bovine (femur) bone material as a function of experimental annealing temperature (annealing time 1 h). Note the pronounced increase of the OH<sup>-</sup> signals and the decrease of the H<sub>2</sub>O signal with increasing treatment temperature

## Cremated Archaeological Samples

We exemplify results on cremated archaeological bone remains from the Bronze Age (Urnfield Culture) of southern Bavaria with long bones from the Eching site and a skull from the Zuchering site.

Figure 15 shows the Fourier transform infrared spectra of seven samples from the Eching locality in the spectral range of the  $\nu_4$  phosphate group bending modes and the OH<sup>-</sup> libration mode at 633 cm<sup>-1</sup>. The seven samples can be separated into two groups. The first group consists of the samples 20\_Eching (black trace) and 14\_Eching (red trace) which show fairly similar FTIR spectra. Their ~567 cm<sup>-1</sup> band is at lower frequencies than that of the second group, and the width of both the 567 cm<sup>-1</sup> band and the 603 cm<sup>-1</sup> band is broad; further, they do not show a well-

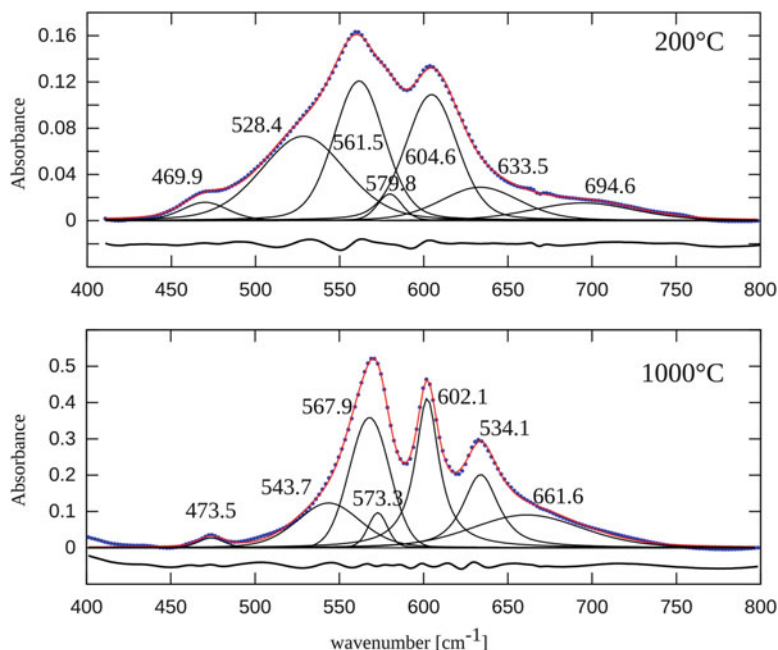
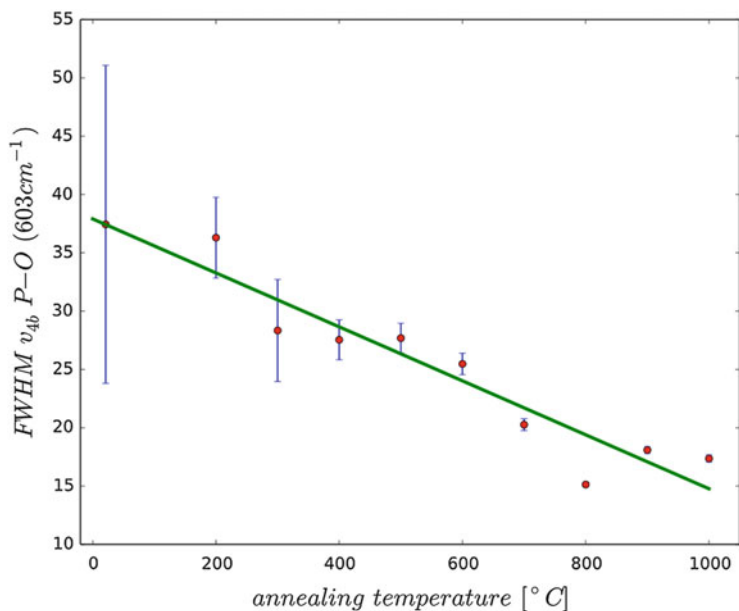


**Fig. 13** Spectral decomposition of the FTIR signal of the  $\nu_4$   $[\text{PO}_4]^{3-}$  vibration bands and the  $\text{OH}^-$  libration band in the  $400\text{ cm}^{-1}$  to  $800\text{ cm}^{-1}$  range into seven contributions for two exemplary states of experimental annealing of bovine femur bone mineral

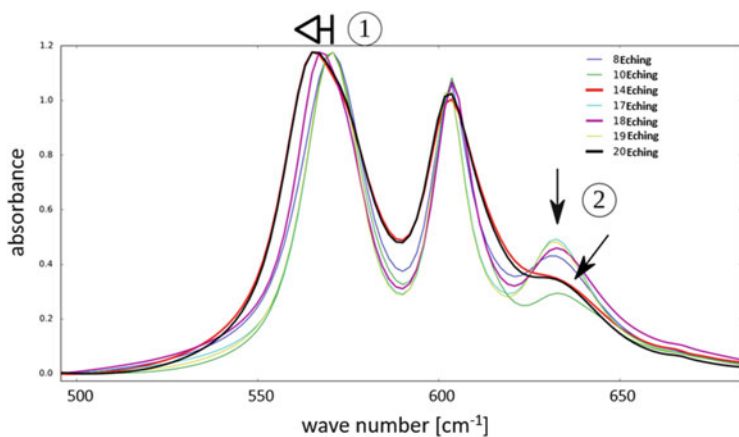
differentiated hydroxyl libration peak at  $632\text{ cm}^{-1}$ . The second group consists of the remaining five samples with narrower peaks for the phosphate bands and a well-differentiated  $\text{OH}^-$  libration band. Correspondingly, the group 2 samples have seen higher cremation temperatures than the group 1 samples.

Table 2 lists the results for the estimated cremation temperature based on Eq. (1) from the spectral decomposition of the P–O bands. For group 1, we estimate a cremation temperature around  $750\text{ }^\circ\text{C}$ , while the group 2 samples are placed between  $1000^\circ$  and  $1150\text{ }^\circ\text{C}$ .

As the XRD of the Eching samples (see below) gave strong indications that cremated bones are typically inhomogeneous with respect to the cremation state, we also investigated a cremated skull from the Zuchering site for which we had visually observed colour differences between the inner and outer side of the cranium. Five samples from the cranium were divided into the inner compact bone layer and the outer compact bone layer (the spongiosa was thus lost). Infrared spectra of the skull sample are shown in Fig. 16; FWHM values of the  $\sim 603\text{ cm}^{-1}$  band and corresponding calculated cremation temperatures are given in Table 2. First of all, the IR data for the single skull are quite variant and indicate a range of cremation temperatures between  $834\text{ }^\circ\text{C} \pm 45\text{ }^\circ\text{C}$  and  $1016\text{ }^\circ\text{C} \pm 20\text{ }^\circ\text{C}$ , and there are significant differences between corresponding inner and outer layers, which are just millimetres apart. In contrast, the estimation of the cremation temperature



**Fig. 14** Correlation of the full width at half maximum (FWHM) of the  $603\text{ cm}^{-1}$  band vs. annealing temperature of experimental cremation (annealing time 1 h)



**Fig. 15** FTIR spectra of archaeological cremated samples from the Urnfield Culture site of Eching (1300–800 BC). The phosphate  $\nu_4$  bending modes are highlighted with changes in the frequency (1) of the  $\sim 567\text{ cm}^{-1}$  band, and the appearance and broadening of the  $\text{OH}^-$  libration mode at  $633\text{ cm}^{-1}$  are indicated (2)

**Table 2** Full width at half maximum of the  $\sim 603 \text{ cm}^{-1}$   $\nu_4$  [PO<sub>4</sub>] infrared absorption band for the archaeological cremated samples from the Eching and Zuchering Urnfield Culture sites, the corresponding calculated cremation temperature from Eq. (1), the cremation temperature estimated from XRD crystallite size (Table 1; Fig. 10) and the cremation temperature estimate from the colour of the specimen on the basis of (Wahl 1981)

Sample	FWHM of the 603 $\text{cm}^{-1}$ P–O band ( $\text{cm}^{-1}$ )	Calculated cremation temperature from Eq. 1 ( $^{\circ}\text{C}$ )	Estimated cremation temperature from XRD line width ( $^{\circ}\text{C}$ )	Estimated cremation temperature after Wahl (1981) ( $^{\circ}\text{C}$ )
20_Eching_222	20.1(1.2)	769(100)	700	
14_Eching_727	20.7(1.3)	743(100)	700	
8_Eching_247	14.4(3)	1015(15)	840	
10_Eching_626	14.3(2)	1020(10)	920	
17_Eching_346	11.6(7)	1136(100)	900	
18_Eching_140	12.74(1.8)	1087(10)	950	
19_Eching_219	11.6(2)	1136(10)	1030	
Zuchering skull				
Outer 1	16.6(7)	920(30)	780	550
Inner 1	18.6(0.98)	834(45)	750	550
Outer 2	15.12(81)	985(35)	920	>800
Inner 2	14.4(4)	1016(20)	1020	>800
Outer 3	15.12(57)	984(25)	800	550–600
Inner 3	15.0(5)	989(25)	740	550–600
Outer 4	17.6(8)	877(35)	740	500–550
Inner 4	20(3)	773(167)	700	500–550
Outer 5	16.5(7)	925(30)	750	550
Inner 5	20(3)	773(130)	700	550

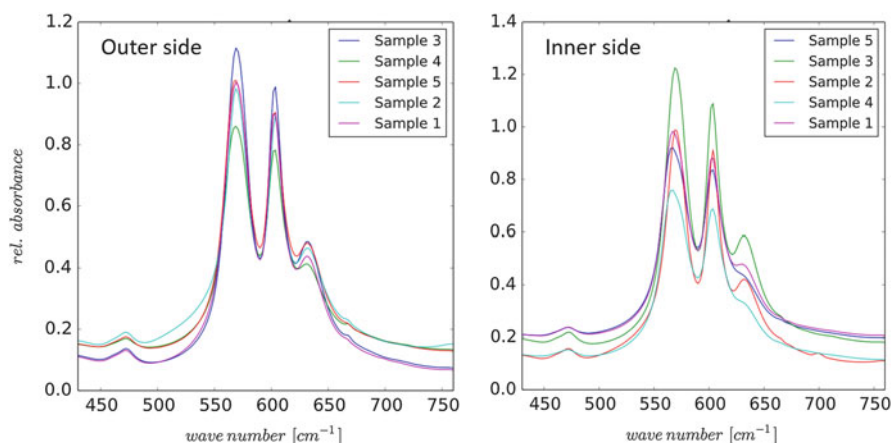


**Fig. 16** FTIR spectra of archaeological cremated skull from the Umfield Culture site of Zuchering (1300–800 BC) covering the phosphate  $\nu_4$  bending modes and the OH<sup>-</sup> libration mode near  $633 \text{ cm}^{-1}$

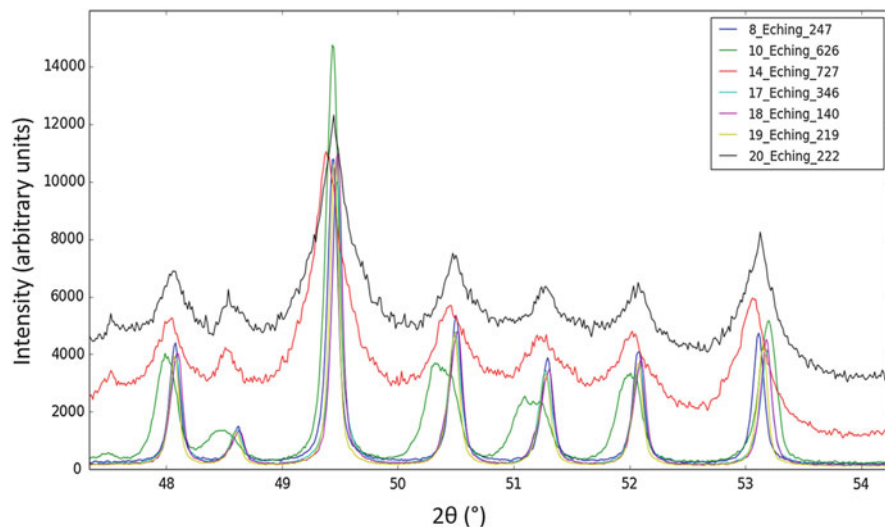


**Fig. 17** XRD patterns of the cremated archaeological samples of the Urnfield Culture Eching locality. Cu-K $\alpha_1$  radiation. The group 1 samples 14\_Eching and 20\_Eching show broad peaks, indicating smaller crystallite sizes and thus lower cremation temperatures than the other samples (group 2). The diffractogram of the 10\_Eching sample indicates a completely different material state than the other group 2 samples

based on the colour of the sample (Wahl 1981) gives much lower temperatures. The estimate of the cremation temperature based on the FWHM of the  $\sim 603\text{ cm}^{-1}$  band may give slightly overestimated values as the correlation in Fig. 14 may not really be linear and flatten off at temperatures  $>700\text{ }^\circ\text{C}$ . However, even a simple interpolation between the data points in Fig. 14 with the FWHM values of the cremated samples indicates temperatures in excess of those based on the method of (Wahl 1981).

The X-ray diffractograms of the Eching samples are compiled in Fig. 17. Here three groups can be distinguished. Like in the FTIR data above, the samples 14\_Eching and 20\_Eching experienced lower cremation temperatures as their XRD peaks are broad. Rietveld refinement (Fig. 18) puts their crystallite sizes to 22 nm (Table 1), which corresponds to  $700\text{ }^\circ\text{C}$  cremation temperature, within limits of error well corresponding to the estimate derived from FTIR above. The group 2 samples have sharper lines with the exception of 10\_Eching. The latter forms a very particular case which cannot be treated with our temperature calibration for XRD (see below). The group 2 samples excluding 10\_Eching show crystallite sizes in the order of 100–190 nm which puts them into the  $800\text{--}1000\text{ }^\circ\text{C}$  range, again corresponding to the FTIR within bounds of error. A representative Rietveld analysis is shown in Fig. 19. The apatite in the 10\_Eching sample appears to have an entirely different structure from what has been encountered so far in fresh, uncremated archeologic and experimentally cremated bone samples. The observed diffraction trace can be fitted with a monoclinic apatite structure (Ikoma et al. 1999), which is able to produce the flat-topped XRD peaks encountered here

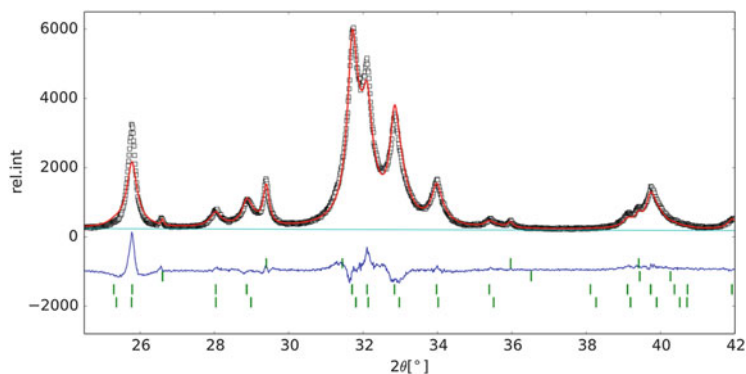


**Fig. 18** Section of the X-ray diffractogram of the 14\_Eching sample. *Red*: observed profile. Cu- $K\alpha_1$  radiation. *Black*: calculated profile. *Blue*: difference curve. *Green*: markers for reflection positions. *From top to bottom*: calcite, quartz, apatite-I and apatite-II. To fit the observed profile with reasonable quality, two apatite phases with slightly different lattice parameters and different microstructural characteristics had to be used

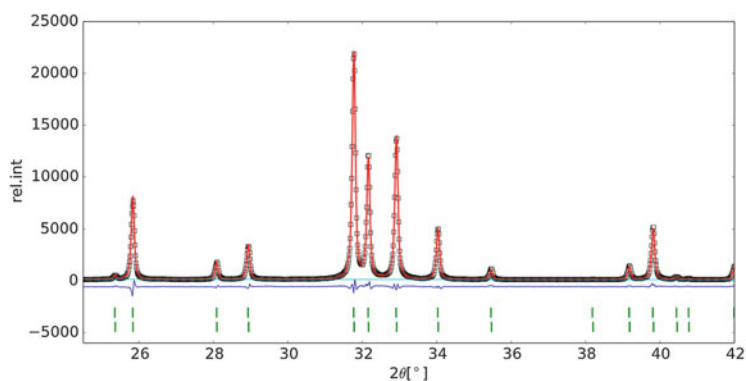


**Fig. 19** Section of the X-ray diffractogram of the 8\_Eching sample. *Red*: observed profile. Cu- $K\alpha_1$  radiation. *Black*: calculated profile. *Blue*: difference curve. *Green*: markers for reflection positions. To fit the observed profile with reasonable quality, two apatite phases with slightly different lattice parameters and different microstructural characteristics had to be used

(Fig. 20). Quartz and calcite impurities from the sediment are also present, which were included in the fit. A possibility to explain the occurrence of the monoclinic symmetry of apatite may be a reaction with ashes or other materials at high temperature in the burning funeral pile. What is clear from the Rietveld refinements of the archaeological sample is that we get pathologic XRD profiles which are not as clearly interpretable as the profiles from fresh or experimentally annealed bone materials. The diffractograms clearly indicate an inhomogeneity in the sample in the sense that apatites with different lattice parameters, different crystallite sizes,

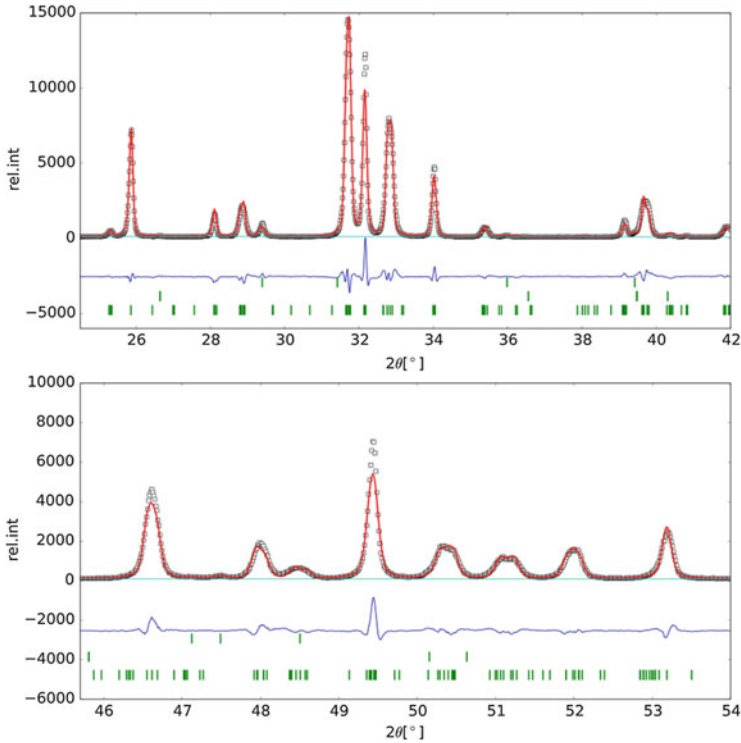


**Fig. 20** Section of the X-ray diffractogram of the 10\_Eching sample. *Red*: observed profile. Cu-K $\alpha_1$  radiation. *Black*: calculated profile. *Blue*: difference curve. *Green*: markers for reflection positions. *From top to bottom*: calcite, quartz, monoclinic apatite. To fit the observed profile with reasonable quality, monoclinic symmetry for apatite had to be used

and microstrain values are needed to model the diffractograms. The origin of inhomogeneity can be attributed to different degrees of cremation intensity. These can result from inhomogeneous temperatures produced by the burning wood logs and tissues, and also from differing lengths of time to which certain bone segments were exposed to the highest cremation temperatures. A similar observation has been made by Stiner et al. (1995) on paleolithic bone material.

Finally, we turn to the XRD results on the Zuchering skull samples. Diffractograms are shown in Fig. 21. The inner parts of samples 4 and 5 have the broadest lines corresponding to the lowest treatment temperatures. From the corresponding crystallite size of 22–23 nm obtained from Rietveld refinement (Table 1), we estimate the cremation temperatures as 700° or slightly above, which is quite consistent with the IR data discussed above. Sample 2 has certainly experienced the highest cremation temperatures, and here we also have fair agreement between FTIR and XRD results. On the whole, we see that the IR calibration overestimates the cremation temperature compared to XRD; for the skull sample 3, we have the greatest discrepancies. There are several potential origins of



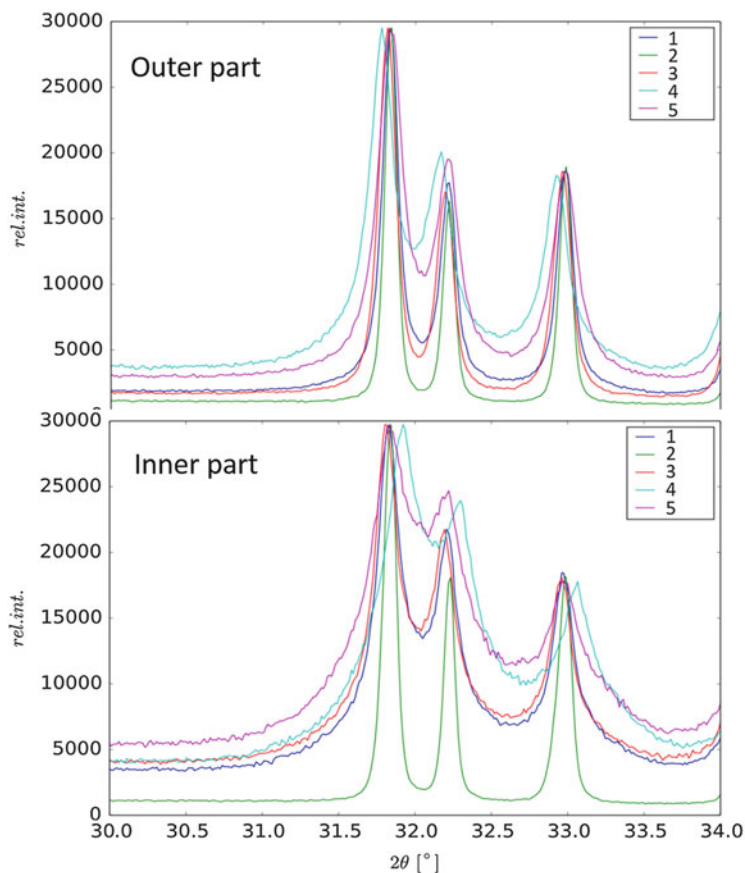


**Fig. 21** Section of the X-ray diffractograms of the Zuchering skull sample comparing outer and inner compact bone layers of the cranium. Cu-K $\alpha_1$  radiation

difference obtained in cremation temperature when applied to archaeological cremated samples. First, our IR calibration is based on the assumption of a linear relationship between the FWHM of the  $\sim 603\text{ cm}^{-1}$  phosphate vibration (Fig. 14) and the annealing temperature. From the XRD evaluation of the experimentally annealed samples, we clearly see that the microstructural change in the material is strongly nonlinear in temperature, with a drastic change between the regimes below and above 600–700 °C (Fig. 10). Second, the archaeological cremated bones are clearly inhomogeneous, and the calibration so far assumes a well-defined average state. However, both the IR and the XRD data are at odds with the cremation temperatures estimated from the colour of the specimens after Wahl (1981).

## Concluding Discussion

Our study of uncremated mammal bone samples from the alpine region covers ages from 7600 to 550 years before present. Only those samples which were of the best quality selected for the isotope studies within FOR1670 were analysed. Visually decomposed bones were avoided completely, and also the surfaces of the bones were mechanically cleaned by grinding away soil and/or decomposed material. The mineralogic state of the thus prepared samples showed only minor signs of diagenetic alteration, and beside bone apatite, the only secondary phase was calcite. The most pronounced change with archeologic age resides in the lattice parameter and in the crystalline domain size in the short dimension of the original bone-apatite platelets; the long direction corresponding to the crystallographic *c*-axis of the apatite appears almost unaffected. From the data, it is clear that other factors such as anatomic variation of the original materials and conditions in the soil play a major role in the diagenetic change of the bone material, masking the changes with burial time. As judged from the lattice parameters, the diagenetic alteration of the original bone mineral, apart from the slight increase in crystallite size, is possibly related to exchange of carbonate by hydroxyl and fluorine.

We established calibration curves from annealing experiments with bovine femur bone material at different temperatures for 1 h annealing time, which were subsequently used to estimate cremation temperatures of archaeological bones based on FTIR spectra and X-ray diffractograms. The experiments indicate that the original bone apatite contains little—if any—OH<sup>-</sup> while carbonate and H<sub>2</sub>O are present. Thus, the bone mineral is a carbonate-hydro-apatite rather than hydroxy-apatite. With increasing annealing temperature, water and carbonate leave the material, and from 600 °C, the bone mineral progressively reacts to form hydroxy-apatite with increasing purity and crystallite size with increasing temperature. We analysed some cremated bones from the Urnfield Culture sites of Eching and Zuchering, southern Bavaria. The analyses clearly indicate that the archaeological cremated bones are inhomogeneous materials, where within fractions of centimetres, the different parts of the samples experienced different cremation temperatures and/or times at temperature. Thus, compared to annealing experiments in furnaces, the conditions within the pile of burning logs and burning tissue are strongly variable locally, in particular towards the outside of the pyre. As the urns typically contain only a small fraction of the skeleton, the selection of bone fragments for burial in the urn might preferentially pick such items which experienced inhomogeneous conditions. The estimated cremation temperatures based on the FTIR and XRD analytical approaches tentatively agree but are still not fully mutually consistent. The IR and XRD data are consistently at odds with the cremation temperatures estimated from the colour of the specimens after Wahl (1981). To discuss the discrepancies between the FTIR and the XRD approaches, we first need to consider that the archaeological cremated bones are clearly inhomogeneous and the calibration so far assumes that a well-defined average state exists. Secondly, our IR calibration so far assumes a linear model relation (Eq. 1) between the FWHM of the ~603 cm<sup>-1</sup> phosphate vibration (Fig. 14) and the

cremation temperature. From the XRD evaluation of the experimentally annealed samples, however, we clearly see that the microstructural change in the material is not simply proportional to temperature: there is a drastic change between the regimes below and above 600–700 °C (Fig. 10). Below this temperature, the IR signal is more sensitive to the change in material state, while in the temperature range above 600 °C, it is the XRD signal which is more sensitive. In the future, more refined models can be produced on the basis of more annealing experiments made to obtain better statistics. Further, cremation experiments must be done in the conditions that exist in a funeral pyre to gain experience on temperature and burning time inhomogeneity. While the evaluation of the diffractograms today is rigorously based on a physical model, the evaluation of spectral components in FTIR spectra is still empirical, and results depend very much on empirical assumptions made on the spectral shape of any single band and the number of bands contributing to the spectral range of overlapping peaks. Future work also definitely needs to address the chemistry and anatomical variability of original bone material within and between species in much more detail than is known at present.

**Acknowledgement** We thank the Deutsche Forschungsgemeinschaft, DFG, for financial support in Forschergruppe FOR1670, projects SCHM930/12-1 and GR959/21-1 and 20-1.

---

## References

- Alexander B, Daulton TL, Genin GM, Lipner J, Pasteris JD, Wopenka B, Thomopoulos S (2012) The nanometre-scale physiology of bone: steric modelling and scanning transmission electron microscopy of collagen–mineral structure. *J Royal Soc Interface* 9:1774–1786
- Balan E, Delattre S, Roche D, Segalen L, Morin G, Guillaumet M, Blanchard M, Lazzeri M, Brouder C, Salje EKH (2011) Line-broadening effects in the powder infrared spectrum of apatite. *Phys Chem Miner* 38:111–122
- Berna F, Matthews A, Weiner S (2004) Solubilities of bone mineral from archaeological sites: the recrystallization window. *J Archaeol Sci* 31:867–882
- Cuisinier F, Bres EF, Hemmerle J, Voegel JC, Frank RM (1987) Transmission electron microscopy of lattice planes in human alveolar bone apatite crystals. *Calcif Tissue Int* 40:332–338
- de Keijser TH, Langford JJ, Mittemeijer EJ, Vogels ABP (1982) Use of the Voigt function in a single-line method for the analysis of X-ray diffraction line broadening. *J Appl Crystallogr* 15:308–314
- de Leeuw NH (2010) Computer simulations of structures and properties of the biomaterial hydroxyapatite. *J Mater Chem* 20:5376–5389
- Elliot JC (2002) Calcium phosphate biominerals. In: Kohn MJ, Rakovan J, Hughes JM (Hrsg) *Phosphates: geochemical, geobiological and material importance. Reviews in mineralogy and geochemistry*, vol 48. Mineralogical Society of America, Washington, DC, pp 631–672
- Enzo S, Bazzoni M, Mazzarello V, Piga G, Bandiera P, Melis P (2007) A study by thermal treatment and X-ray powder diffraction on burnt fragmented bones from tombs II, IV and IX belonging to the hypogeic necropolis of “Sa Figu” near Ittiri, Sassari (Sardinia, Italy). *J Archaeol Sci* 34:1731–1737
- Galeano S, García-Lorenzo ML (2014) Bone mineral change during experimental calcination: an X-ray diffraction study. *J Forensic Sci* 59:1602–1606
- Gernaey AM, Waite ER, Collins MJ, Craig OE, Sokol RJ (2001) Survival and interpretation of archaeological proteins. In Brothwell DR, Pollard AM (Hrsg) *Handbook of archaeological science*. Wiley, Chichester: 323–329

- Gonzalez-Diaz PF, Hidalgo A (1976) Infrared spectra of calcium apatites. *Spectrochim Acta A Mol Spectrosc* 32A:1119–1124
- Gonzalez-Diaz PF, Santos M (1977) On the hydroxyl ions in apatites. *J Solid State Chem* 22:193–199
- Grunenwald A, Keyser C, Sautereau AM, Crubézy E, Ludes B, Drouet C (2014) Novel contribution on the diagenetic physicochemical features of bone and teeth minerals, as substrates for ancient DNA typing. *Anal Bioanal Chem* 406:4691–4704
- Grupe G, Harbeck M, McGlynn GC (2015) *Prähistorische Anthropologie*. Springer, Berlin
- Harbeck M, Schleuder R, Schneider J, Wiechmann I, Schmahl WW, Grupe G (2011) Research potential and limitations of trace analyses of cremated remains. *Forensic Sci Int* 204:191–200
- Hedges REM (2002) Bone diagenesis: an overview of processes. *Archaeometry* 44:319–328
- Ikoma T, Yamazaki A, Nakamura S, Akao M (1999) Preparation and structure refinement of monoclinic hydroxyapatite. *J Solid State Chem* 144:272–276
- Jäger C, Welzel T, Meyer-Zaika W, Epple M (2006) A solid-state NMR investigation of the structure of nanocrystalline hydroxyapatite. *Magn Reson Chem* 44:573–580
- Landis WJ, Jacquet R (2013) Association of calcium and phosphate ions with collagen in the mineralization of vertebrate tissues. *Calcif Tissue Int* 93:329–337
- Lebon M, Reiche I, Frohlich F, Bahain J, Falgueres C (2008) Characterization of archaeological burnt bones: contribution of a new analytical protocol based on derivative FTIR spectroscopy and curve fitting of the  $\nu_1$  and  $\nu_3$   $\text{PO}_4$ . *Anal Bioanal Chem* 392:1479–1488
- Lee-Thorp J, Sponheimer M (2003) Three case studies used to reassess the reliability of fossil bone and enamel isotope signals for paleodietary studies. *J Anthropol Archaeol* 23:208–216
- LeGeros RZ, Trautz OR, Legeros JP, Klein E, Shirra WP (1967) Apatite crystallites: effects of carbonate on morphology. *Science* 155:1409–1411
- LeGeros RZ, Trautz OR, Legeros JP, Klein E (1968) Carbonate substitution in the apatite structure. *Bull Soc Chim Fr* 4:1712–1718
- Loong CK, Rey C, Kuhn LT, Combes C, Wu Y, Chen SH, Glimcher MJ (2000) Evidence of hydroxyl-ion deficiency in bone apatites: an inelastic neutron-scattering study. *Bone* 26:599–602
- McKinley J (2016) Complexities of the ancient mortuary rite of cremation: an osteoarchaeological conundrum. In: Grupe G, McGlynn GC (eds) *Isotopic landscapes in bioarchaeology*. Springer, Berlin, pp. 17–41
- Mittemeijer EJ, Welzel U (eds) (2012) *Modern diffraction methods*. Wiley-VCH, Weinheim, 528p
- Munro LE, Longstaffe FJ, White CD (2008) Effects of heating on the carbon and oxygen-isotope compositions of structural carbonate in bioapatite from modern deer bone (Beyond documenting diagenesis: the fifth international bone diagenesis workshop). *Palaeogeogr Palaeoclimatol Palaeoecol* 266:142–150
- Nielsen-Marsh CM, Hedges REM (2000) Patterns of diagenesis in bone I: the effects of site environments. *J Archaeol Sci* 27:1139–1150
- Nielsen-Marsh CM, Gernaey A, Turner-Walker G, Hedges REM, Pike A, Collins MJ (2000) The chemical degradation of bone. In: Cox M, Mays S (eds) *Human osteology in archaeology and forensic science*. Greenwich Medical Media, London, pp. 439–454
- Olsen J, Heinemeier J, Bennike P, Krause C, Hornstrup KM, Thrane H (2008) Characterisation and blind testing of radiocarbon dating of cremated bone. *J Archaeol Sci* 35:791–800
- Pasteris JD, Wopenka B, Freeman JJ, Rogers K, Valsami-Jones E, van der Houwen AM, Silva MJ (2004) Lack of OH in nanocrystalline apatite as a function of degree of atomic order: implications for bone and biomaterials. *Biomaterials* 25:229–238
- Pecharsky VK, Zavalij PY (2003) *Fundamentals of powder diffraction and structural characterization of materials*. Springer, New York, 741p
- Pedone A, Corno M, Civalieri B, Malavasi G, Menziani C, Segrea U, Ugliengo P (2007) An ab initio parameterized interatomic force field for hydroxyapatite. *J Mater Chem* 17:2061–2068
- Person A, Bocherens H, Saliege JF, Paris F, Zeitoun V, Gerard M (1995) Early diagenetic evolution of bone phosphate—an X-ray diffractometry analysis. *J Archaeol Sci* 22:211–221
- Peters F, Schwarz K, Epple M (2000) The structure of bone studied with synchrotron X-ray diffraction, X-ray absorption spectroscopy and thermal analysis. *Thermochim Acta* 361:131–138

- Piga G, Malgosa A, Thompson TJU, Enzo S (2008) A new calibration of the XRD technique for the study of archaeological burned human remains. *J Archaeol Sci* 35:2171–2178
- Piga G, Thompson TJU, Malgosa A, Enzo S (2009a) The potential of X-Ray diffraction in the analysis of burned remains from forensic contexts. *J Forensic Sci* 54:3534–3539
- Piga G, Santos-Cubedo A, Moya Sola S, Brunetti A, Malgosa A, Enzo S (2009b) An X-ray diffraction (XRD) and X-ray fluorescence (XRF) investigation in human and animal fossil bones from Holocene to Middle Triassic. *J Arch Sci* 36:857–1868
- Piga G, Solinas G, Thompson TJU, Brunetti A, Malgosa A, Enzo S (2013) Is X-ray diffraction able to distinguish between animal and human bones? *J Archaeol Sci* 40:778–785
- Pucéat E, Reynard B, Lécuyer C (2004) Can crystallinity be used to determine the degree of chemical alteration of biogenic apatites? *Chem Geol* 205:83–97
- Rey C, Collins B, Goehl T, Dickson IR, Glimcher MJ (1989) The carbonate environment in bone mineral: A resolution-enhanced fourier transform infrared spectroscopy study. *Calcif Tissue Int* 45:157–164
- Rey C, Combes C, Drouet C, Glimcher MJ (2009) Bone mineral: update on chemical composition and structure. *Osteoporos Int* 20:1013–1021
- Rey C, Combes C, Drouet C, Cazalbou S, Grossin D, Brouillet F, Sarda S (2014) Surface properties of biomimetic nanocrystalline apatites; applications in biomaterials. *Prog Cryst Growth Charact Mater* 60:63–73
- Rey C, Miquel JL, Facchini L, Legrand AP, Glimcher MJ (1995) Hydroxyl groups in bone mineral. *Bone* 16:583–586
- Rey C, Renugopalakrishnan V, Collins B, Glimcher MJ (1991) Fourier transform infrared spectroscopic study of carbonate ions in bone mineral during aging. *Calcif Tissue Int* 49:251–258
- Rey C, Shimizu M, Collins B, Glimcher MJ (1990) Resolution-enhanced fourier transform infrared spectroscopy study of the environment of phosphate ions in the early deposits of a solid phase of calcium-phosphate in bone and enamel, and their evolution with age. I: Investigations in the  $\nu_4$ PO<sub>4</sub> domain. *Calcif Tissue Int* 46:384–394
- Reznikov N, Shahar R, Weiner S (2014) Three-dimensional structure of human lamellar bone: the presence of two different materials and new insights into the hierarchical organization. *Bone* 59:93–104
- Rho J-Y, Kuhn-Spearing L, Zioupos P (1998) Mechanical properties and the hierarchical structure of bone. *Med Eng Phys* 20:92–102
- Rietveld H (1969) A profile refinement method for nuclear and magnetic structures. *J Appl Crystallogr* 2:65–71
- Rodriguez-Carvajal J (1993) Recent advances in magnetic structure determination by neutron powder diffraction. *Phys B Condens Matter* 192:55–69
- Rodriguez-Carvajal J, Roisnel T (2004) Line broadening analysis using FullProf: determination of microstructural properties. *Mater Sci Forum* 443:123–126
- Rogers KD, Beckett S, Kuhn S, Chamberlain A, Clement J (2010) Contrasting the crystallinity indicators of heated and diagenetically altered bone mineral. *Palaeogeogr Palaeoclimatol Palaeoecol* 296:125–129
- Rogers KD, Daniels P (2002) An X-ray diffraction study of the effects of heat treatment on bone mineral microstructure. *Biomaterials* 23:2577–2585
- Schmahl WW, Kocis B, Toncala A, Grupe GJ (2016) Mineralogic characterisation of archaeological bone. In: Grupe G, McGlynn GC (eds) *Isotopic landscapes in bioarchaeology*. Springer, Berlin, pp. 17–41
- Schurr MR, Hayes RG, Cook DC (2008) Thermally induced changes in the stable carbon and nitrogen isotope ratios of charred bones. In: Schmidt CW, Symes SA (eds) *The analysis of burned human remains*. Academic Press, London, pp 95–108
- Schwarz HP, McNally EA, Botton GA (2014) Dark-field transmission electron microscopy of cortical bone reveals details of extrafibrillar crystals. *J Struct Biol* 188:240–248
- Shemesh A (1990) Crystallinity and diagenesis of sedimentary apatites. *Geochim Cosmochim Acta* 54:2433–2438
- Shinomiya T, Shinomiya K, Orimoto C, Minami T, Tohno Y, Yamada MO (1998) In- and out-flows of elements in bones embedded in reference soils. *Forensic Sci Int* 98:109–118

- Sillen A (1989) Diagenesis of the inorganic phase of cortical bone. In Price TD (Hrsg) *The chemistry of prehistoric human bone*. Cambridge University Press, New York, pp 211–229
- Sponheimer M, de Ruiter D, Lee-Thorp J, Späth A (2005) Sr/Ca and early hominin diets revisited: new data from modern and fossil tooth enamel. *J Hum Evol* 48:147–156
- Stathopoulou ET, Psycharis V, Chryssikos GD, Gionis V, Theodorou G (2008) Bone diagenesis: new data from infrared spectroscopy and X-ray diffraction. *Palaeogeogr Palaeoclimatol Palaeoecol* 266:168–174
- Stiner MC, Kuhn SL, Weiner S, Bar-Yosef O (1995) Differential burning, recrystallization, and fragmentation of archaeological bone. *J Archaeol Sci* 22:223–237
- Surovell TA, Stiner M (2001) Standardizing infra-red measures of bone mineral crystallinity: an experimental approach. *J Archaeol Sci* 28:633–642
- Thompson P, Cox DE, Hastings JB (1987) Rietveld refinement of Debye-Scherrer synchrotron X-ray data from  $Al_2O_3$ . *J Appl Crystallogr* 20:79–83
- Tonegawa T, Ikoma T, Yoshioka T, Hanagata N, Tanaka J (2010) Crystal structure refinement of A-type carbonate apatite by X-ray powder diffraction. *J Mater Sci* 45:2419–2426
- Trueman CN, Privat K, Field J (2008) Why do crystallinity values fail to predict the extent of diagenetic alteration of bone mineral? *Palaeogeogr Palaeoclimatol Palaeoecol* 266:160–167
- Tütken T, Vennemann TW, Pfretzschner H-U (2008) Early diagenesis of bone and tooth apatite in fluvial and marine settings: constraints from combined oxygen isotope, nitrogen and REE analysis. *Palaeogeogr Palaeoclimatol Palaeoecol* 266:254–268
- Turner-Walker G (2008) The chemical and microbial degradation of bones and teeth. In Pinhasi R, Mays S (Hrsg) *Advances in human paleopathology*. Wiley, Chichester, pp 3–29
- Vandecastelaere N, Rey C, Drouet C (2012) Biomimetic apatite-based biomaterials: on the critical impact of synthesis and post-synthesis parameters. *J Mater Sci Mater Med* 23:2593–2606
- Wahl J (1981) Beobachtungen zur Verbrennung menschlicher Leichname. *Archäologisches Korrespondenzblatt* 11:271–279
- Wang Y, Von Euw S, Fernandes FM, Cassignon S, Selmane M, Laurent G, Pehau-Arnaudet G, Coelho C, Bonhomme-Courty L, Giraud-Guille M-M, Babonneau F, Azais T, Nassif N (2013) Water-mediated structuring of bone apatite. *Nat Mater* 12:1144–1153
- Wegst UGK, Bai H, Saiz E, Tomsia AP, Ritchie RO (2015) Bioinspired structural materials. *Nat Mater* 14:23–36
- Weiner S, Bar-Yosef O (1990) State of preservation of bones from the prehistoric sites in the near East: a survey. *J Archaeol Sci* 17:187–196
- Weiner S, Goldberg P, Bar-Yosef O (1993) Bone preservation in Kebara Cave, Israel using on-site Fourier-transform infrared spectroscopy. *J Archaeol Sci* 20:613–627
- Weiner S, Traub W, Wagner HD (1999) Lamellar bone: structure-function relations. *J Struct Biol* 126:241–255
- Wilson RM, Elliot JC, Dowker SEP (1999) Rietveld refinement of the crystallographic structure of human dental enamel apatites. *Am Mineral* 84:1406–1414
- Wilson RM, Elliot JC, Dowker SEP, Rodriguez-Lorenzo LM (2005) Rietveld refinements and spectroscopic studies of the structure of Ca-deficient apatite. *Biomaterials* 26:1317–1327
- Wopenka B, Pasteris JD (2005) A mineralogical perspective on the apatite in bone. *Mater Sci Eng C* 25:131–143
- Wright LE, Schwarcz HP (1996) Infrared and isotopic evidence for diagenesis of bone apatite at Dos Pilas, Guatemala: palaeodietary implications. *J Archaeol Sci* 23:933–944
- Yerramshetty JS, Akkus O (2008) The associations between mineral crystallinity and the mechanical properties of human cortical bone. *Bone* 42:476–482
- Yi H, Balan E, Gervais C, Ségalen L, Blanchard M, Lazzeri M (2014) Theoretical study of the local charge compensation and spectroscopic properties of B-type carbonate defects in apatite. *Phys Chem Miner* 4:347–359
- Yi H, Balan E, Gervais C, Segalen L, Fayon F, Roche D, Person A, Morin G, Guillaumet M, Blanchard M, Lazzeri M, Babonneau F (2013) A carbonate-fluoride defect model for carbonate-rich fluorapatite. *Am Mineral* 98:1066–1069